Magnetic forces and stationary electron flow in a three-terminal semiconductor quantum ring

2010 J. Phys.: Condens. Matter 22 215801

(http://iopscience.iop.org/0953-8984/22/21/215801)

IOP Publishing Journal of Physics: Condensed Matter

J. Phys.: Condens. Matter **22** (2010) 215801 (13pp) doi:10.1088/0953-8984/22/21/215801

Magnetic forces and stationary electron flow in a three-terminal semiconductor quantum ring

M R Poniedziałek and B Szafran

Faculty of Physics and Applied Computer Science, AGH University of Science and Technology, aleja Mickiewicza 30, 30-059 Kraków, Poland

Received 16 March 2010
Published 5 May 2010
Online at stacks.iop.org/JPhysCM/22/215801

Abstract

We study stationary electron flow through a three-terminal quantum ring and describe effects due to deflection of electron trajectories by classical magnetic forces. We demonstrate that generally at high magnetic field (B) the current is guided by magnetic forces to follow a classical path, which for $B > 0$ leads via the left arm of the ring to the left output terminal. The transport to the left output terminal is blocked for narrow windows of magnetic field for which the interference within the ring leads to formation of wavefunctions that are only weakly coupled to the output channel wavefunctions. These interference conditions are accompanied by injection of the current to the right arm of the ring and by appearance of sharp peaks of the transfer probability to the right output terminal. We find that these peaks at high magnetic field are attenuated by thermal widening of the transport window. We also demonstrate that the interference conditions that lead to their appearance vanish when elastic scattering within the ring is present. The clear effect of magnetic forces on the transfer probabilities disappears along with Aharonov–Bohm oscillations in a chaotic transport regime that is found for rings whose width is larger than the width of the channels.

(Some figures in this article are in colour only in the electronic version)

1. Introduction

Phase-coherent electron transport in mesoscopic [1–3] and nanoscale [4–8] rings results in appearance of Aharonov–Bohm [9] conductance oscillations in external magnetic field. These conductance oscillations are extensively studied in the context of scanning gate spectroscopy [10], spin–orbit coupling for both electrons [11, 12] and holes [13], Aharonov–Bohm interferometry [14] including electron self-interference [15], violation of Onsager symmetry [16], and magnetic forces [17–20].

The deflection of electron trajectories by magnetic forces in two-terminal quantum rings was previously studied by time-dependent wavepacket simulations [17], which indicated that in the presence of external perpendicular magnetic field the electron packet is preferentially injected into one of the arms of the ring, which reduces the Aharonov–Bohm interference of electron waves meeting near the exit to the output lead. A time-dependent simulation was also used to describe the transport through a three-terminal quantum ring [18], which demonstrated that the Lorentz force—besides the reduction of the Aharonov–Bohm oscillations at high field—results in a distinct imbalance of the wavepacket transfer probabilities to the two output leads. Such an imbalance of conductance of two output leads was indeed found in a recent experiment [20].

A three-terminal quantum ring is a basic element [21] for construction of ring arrays that are proposed for implementation of quantum logic operations [22, 23] using spin–orbit interactions. In these structures [21–23] the direction of the charge current is determined by the electron spin orientation. Magnetic forces [20] can provide a mean of external control of the current flow.

The time-dependent simulations as previously performed for three-terminal rings [18, 19] are based on a relatively straightforward procedure that indicates in a clear way the electron trajectories across the nanostructure. The charge transfer is a time-dependent process only in selected experiments; cf. the single-electron injection into the quantum ring [15] realized according to the single-electron pump technique based on the Coulomb blockade [24]. The standard

experiments measure the current due to the stationary electron flow at the Fermi level, which is therefore of a more basic interest than the wavepacket dynamics. With the time-dependent approach one can in principle approach the monoenergetic time-independent limit, increasing the spatial spread of the wavepacket in the initial condition, but the latter is limited by the necessarily finite size of the computational box.

The purpose of the present paper is to describe the effect of magnetic forces on electron transport through a three-terminal ring in Hamiltonian eigenstates. We find that at high magnetic field the electron flow follows the path determined by the Lorentz force—one of the arms of the ring is selected by the current which leaves the ring to the nearest output channel. However, exceptions to this rule are found for resonant interference conditions that block the transport to the output channel that is preferred by magnetic forces. This blockade is accompanied by anomalous (nonclassical) injection of the current to the ring and by appearance of peaks of the transfer probability to the other output channel. We study the thermal stability of this anomalous current injection, the influence of the elastic scatterers for the resonant interference and effects of magnetic forces in the chaotic transport regime. We also study oscillations of the current circulation, which turn out to be more thermally stable than the oscillations of the transfer probabilities. Orientation of the currents circulating inside the ring determines the sign of the magnetic dipole moment that they generate. The magnetization oscillations due to the Aharonov–Bohm effect were so far measured for mesoscopic open quantum rings [25] and for large ensembles of closed nanorings [26].

2. Theory

2.1. Model system

The geometry of the studied system is depicted in figure 1. The inner and outer radii of the ring are 88 nm and 154 nm, respectively. The channels are assumed to be 68 nm wide. We treat the straight channel connected to the ring from below as the input terminal. The contacts to the input and the output channels are spaced by 120° angles. The output channels are bent twice under the angle of 30° to acquire vertical orientation at the end of the computational box, which allows for a uniform treatment of incoming and outgoing wavefunctions and currents (see below).

We adopt a two-dimensional model and assume that the magnetic field is oriented perpendicular to the plane of confinement. We consider the electron Hamiltonian in the form

$$H = (-\mathrm{i}\hbar\nabla + e\mathbf{A}(\mathbf{r}))^2/2m^* + V(x, y) \tag{1}$$

where $V(x, y)$ is the confinement potential—assumed zero within the channels (white area in figure 1) and $V_0 = 200$ meV outside (the grey area in figure 1). The potential offset V_0 corresponds to channels made of GaAs embedded in an $Al_{0.45}Ga_{0.55}As$ matrix. In equation (1) $-e$ is the electron charge ($e > 0$) and $m^* = 0.067m_0$ is the GaAs electron band effective mass.

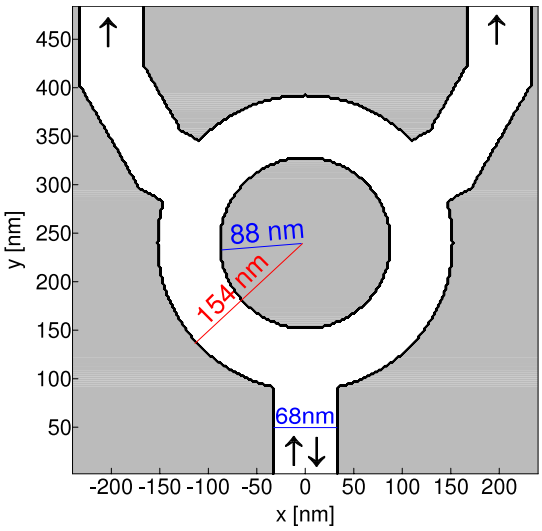

Figure 1. Schematic drawing of the three-terminal ring. The confinement potential is zero inside the channels and 200 meV outside (grey area). The channel width is 68 nm; the inner and outer radii of the ring are 88 nm and 154 nm, respectively. The channel connected to the ring from below is the input lead.

2.2. Hamiltonian discretization

For the description of the stationary charge transport through the system we need to determine the Hamiltonian (1) eigenfunctions for the electron coming from the input channel. We employ the finite difference approach with a square computational box of side length 482 nm (see figure 1) on a grid of 241 × 241 points with mesh spacings $\Delta x = \Delta y = 2$ nm. The results presented below are unaffected when one enlarges the computational box to cover a larger part of the input and the output channels. We use the Wilson [27] type of discretization of the kinetic energy operator in a version adapted by Governale and Ungarelli [28] for semiconductor nanostructures. The discretization is consistent with the original Hamiltonian (tends to it in the $\Delta x = 0$ limit) and gauge-invariant (accounts for the gauge transformation $\mathbf{A} \to \mathbf{A} + \nabla\chi(\mathbf{r})$ inducing wavefunction phase change $\Psi(\mathbf{r}) \to \exp(-\frac{\mathrm{i}e}{\hbar}\chi(\mathbf{r}))\Psi(\mathbf{r})$). The kinetic energy operator [28] acting on a wavefunction defined on a mesh yields

$$\frac{1}{2m^*}(\mathbf{p} + e\mathbf{A})^2\Psi_{\mu,\nu} = \frac{\hbar^2}{2m^*\Delta x^2}(4\Psi_{\mu,\nu} - C_y\Psi_{\mu,\nu-1} - C_y^*\Psi_{\mu,\nu+1} - C_x\Psi_{\mu-1,\nu} - C_x^*\Psi_{\mu+1,\nu}), \tag{2}$$

where $\Psi_{\mu,\nu} = \Psi(x_\mu, y_\nu)$, $C_y = \exp[-\mathrm{i}\frac{e}{\hbar}\Delta x A_y]$, and $C_x = \exp[-\mathrm{i}\frac{e}{\hbar}\Delta x A_x]$. We apply the Lorentz gauge $\mathbf{A} = (A_x, A_y, 0) = (0, Bx, 0)$, for which the mesh Hamiltonian eigenequation reads

$$H\Psi_{\mu,\nu} = \frac{\hbar^2}{2m^*\Delta x^2}(4\Psi_{\mu,\nu} - C_y\Psi_{\mu,\nu-1} - C_y^*\Psi_{\mu,\nu+1} - \Psi_{\mu-1,\nu} - \Psi_{\mu+1,\nu}) + V_{\mu,\nu}\Psi_{\mu,\nu} = E\Psi_{\mu,\nu}. \tag{3}$$

We find the energy E by solution of the boundary problem in the incoming lead (see section 2.3), then equation (3) is solved as a system of linear equations.

2.3. Boundary conditions

The confinement potential in both the input and the output channels depends only on the x coordinate. The chosen gauge allows for separation of the x and y coordinates in the Hamiltonian eigenfunctions

$$\Psi(x, y) = \exp(\mathrm{i}ky)\psi_n^k(x), \tag{4}$$

with the wavevector k. In the absence of the magnetic field the nth Hamiltonian eigenstate of a $w = 68$ nm wide channel has the energy $E_n = n^2\pi^2/2m^*w^2 = 1.21n^2$ meV. We consider the transport limited to the lowest $n = 1$ subband and skip the subscript n in the following. Only the electrons with wavevector exceeding $k \simeq 0.08$ nm^{-1} have enough energy to be scattered to higher subbands. We restrict our discussion to lower values of k. According to the Landauer–Büttiker approach [29] in the single subband transport the conductance G is simply proportional to the transfer probability $G = \frac{2e^2}{h}T$.

We first determine the boundary conditions for the incoming lead. We assume $\nu = 1$ (lowest row of the mesh in the computational box) and plug

$$\Psi_{\mu,\nu\pm1} = \exp(\pm\mathrm{i}k\Delta x)\psi_\mu^k \tag{5}$$

into equation (3) to obtain the one-dimensional eigenequation

$$\begin{aligned}\frac{\hbar^2}{2m^*\Delta x^2}(2\psi_\mu^k - \psi_{\mu-1}^k - \psi_{\mu+1}^k) \\ + \frac{\hbar^2}{m^*\Delta x^2}\left(1 - \cos\left(k\Delta x + \frac{e}{\hbar}Bx\Delta x\right)\right)\psi_\mu^k \\ + V_\mu\psi_\mu^k = E\psi_\mu^k.\end{aligned} \tag{6}$$

Equation (6) provides the energy E that is used in the main equation (3) as well as eigenfunctions corresponding to incident ($k > 0$) and reflected ($k < 0$) electrons that are used for setting the Dirichlet boundary condition for equation (3) at the bottom of the computational box

$$\Psi_{\mu,\nu=1} = c_k\psi_\mu^k + c_{-k}\psi_\mu^{-k}, \tag{7}$$

where the amplitudes of the incident c_k and reflected c_{-k} wavefunctions are determined in a manner described in section 2.5.

Boundary condition (7) guarantees that the energy density $H\Psi(x, y)/\Psi(x, y) = E$ in the incoming lead and within the ring as found from equation (3) are equal. In order to match the energy density inside the ring the wavevectors in the output channels (see equation (4)) in non-zero B must be different from k. Within the channels the confinement potential is zero, therefore equal energy density means equal kinetic energy density. The kinetic energy operator is proportional to the square of the kinetic momentum $\Pi^2 = (p + e\mathbf{A})^2 = \Pi_x^2 + \Pi_y^2 = -\hbar^2\frac{\partial^2}{\partial x^2} + (-\mathrm{i}\hbar\frac{\partial}{\partial y} + eBx)^2$. Since the input and the output channels have the same width, the energy density is matched for the wavevectors in the left k_l and right k_r output leads related to the wavevector of the incoming lead k as $k_\mathrm{l} = k - \frac{eB}{\hbar}x_\mathrm{l}$, and $k_\mathrm{r} = k - \frac{eB}{\hbar}x_\mathrm{r}$, where x_l and x_r are positions of the axes of the left and right output leads ($x_\mathrm{r} = -x_\mathrm{l} =$ 200 nm). Accordingly, for the boundary condition at the top of the computational box we use

$$\Psi_{\mu,\nu+1} = \Psi_{\mu,\nu}\exp(\mathrm{i}k'\Delta x), \tag{8}$$

where $k' = k_\mathrm{l}$ for $x < 0$ and $k' = k_\mathrm{r}$ for $x > 0$. This condition is introduced into equation (3) for the top end of the computational box ($\nu = 241$).

On the left and right edges of the computational box we introduce an infinite potential barrier which amounts to putting $\Psi_{\mu-1,\nu} = 0$ or $\Psi_{\mu+1,\nu} = 0$ in equation (3) for mesh points at the left and right ends of the box, respectively.

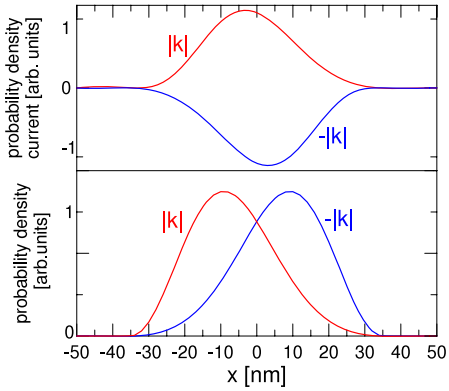

Figure 2. Probability density (lower panel) and probability density current (upper panel) across the incoming lead for the incident $\Psi^{|k|}(x)$ and backscattered $\Psi^{-|k|}(x)$ electron eigenfunctions for $|k| = 0.05$ nm^{-1} at $B = 1$ T.

2.4. Backscattering probability

The vertical component of the probability density current in the incoming lead

$$j(x) = \frac{\hbar}{m^*}\,\mathrm{Im}\left(\Psi^*\frac{\partial\Psi}{\partial y}\right) + \frac{e}{m^*}A_y, \tag{9}$$

is a superposition $j(x) = j^k(x) + j^{-k}(x)$ of the incident current

$$j^k(x) = \frac{\hbar}{m^*}|c_k|^2|\psi^k(x)|^2(\hbar k + eBx) \tag{10}$$

and the backscattered one

$$j^{-k}(x) = \frac{\hbar}{m^*}|c_{-k}|^2|\psi^{-k}(x)|^2(-\hbar k + eBx). \tag{11}$$

Figure 2 shows the probability density and probability density current across the incoming lead for the incident (k) and reflected ($-k$) waves for $k = 0.05$ nm^{-1} and $B = 1$ T. Probability densities are shifted from the axis of the lead to the left with respect to the direction of the current flow in consistence with the Lorentz force orientation. The backscattering probability is evaluated as a ratio of the current fluxes integrated across the input channel,

$$R = \frac{\int \mathrm{d}x\, j^{-k}(x)}{\int \mathrm{d}x\, j^k(x)}. \tag{12}$$

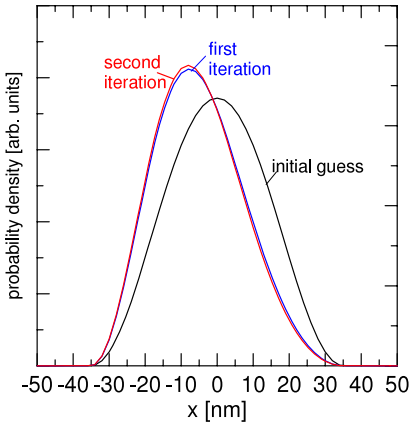

Figure 3. The probability density in the incoming lead $c_k\Psi^k(x) + c_{-k}\Psi^{-k}(x)$ in the initial guess $c_k = c_{-k}$ and in the subsequent iterations of the self-consistent procedure (see text). Parameters are the same as in figure 2.

For the axis of the incoming lead $x = 0$, the solutions of eigenequation (6) with opposite k are related as $\psi^k(x) = \psi^{-k}(-x)$, which implies that (1) the backscattering probability is simply

$$R = \left|\frac{c_{-k}}{c_k}\right|^2, \tag{13}$$

and (2) both the incident and reflected wavefunctions correspond to the same average value of Π_y^2.

Solution of the system of equation (6) gives the wavefunction in the entire system. Now our task is to extract $c_{\pm k}$, i.e. the contributions of the incident and backscattered wavefunctions. For this purpose we consider two points in the incoming lead near the bottom of the computational box. We typically take two lowest points of the axis of the lead ($\mu = 120, \nu = 1$) and ($\mu = 120, \nu = 2$); the results are not affected by a specific choice of these points. The wavefunction for $\nu = 1$ is given by equation (7) and for $\nu = 2$ we have

$$\Psi^k_{\mu,\nu=2} = c_k\psi^k_\mu \exp(\mathrm{i}k\Delta x) + c_{-k}\psi^{-k}_\mu \exp(-\mathrm{i}k\Delta x). \tag{14}$$

The eigenfunctions ψ^k_μ, ψ^{-k}_μ are determined from equation (6). Formulae (7) and (14) form the system of equations for c_k and c_{-k}.

2.5. Self-consistence for the amplitudes of the incident and reflected wavefunctions

For non-zero B the Hamiltonian (6) depends on the sign of the wavevector, and the eigenfunctions for $\pm k$ are different. We need to assume some initial values for c_k and c_{-k} to set the boundary condition (7) for the system of equation (3). Solution of equation (3) gives the wavefunction in the entire computational box, including the incoming lead, of which c_k and c_{-k} can be extracted. The procedure to determine c_k and c_{-k} is performed in a self-consistent iteration with $c_k = c_{-k} = \frac{1}{\sqrt{2}}$ assumed as the initial guess. The iteration converges quite fast. Figure 3 shows the charge density across the incoming lead for $k = 0.05$ nm^{-1} at $B = 1$ T. The final result differs considerably from the initial guess but the results of the second iteration only slightly differ from the first one. For parameters applied in figure 3 the result for the backscattering probability $R = |c_{-k}|^2/|c_k|^2$ converges from one (for the initial guess) to 0.021. Naturally, the iteration affects the results in the entire computational box.

Note that by the initial guess $c_k = c_{-k}$ one assumes that the wavefunction in the incoming lead is symmetric with respect to its axis. For non-zero B this is the case only when backscattering probability reaches 100%.

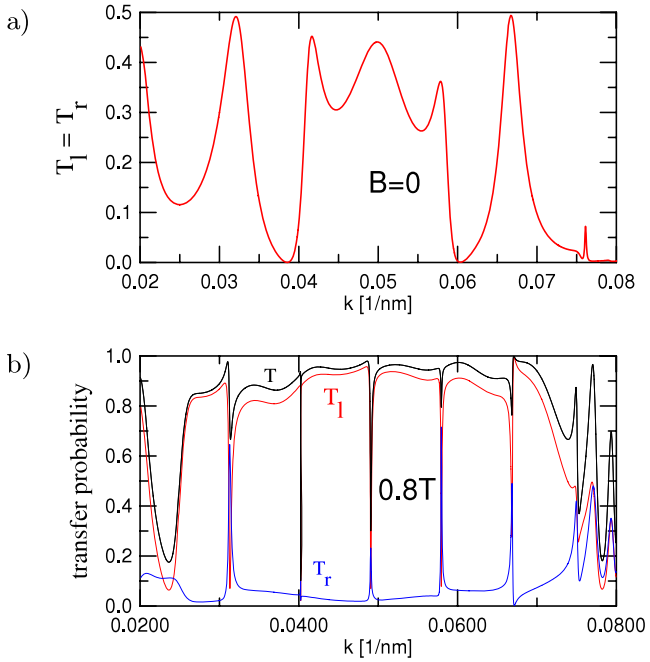

Figure 4. Transfer probabilities to the left T_l and right T_r output channels and their sum T as functions of the incident wavevector k for $B = 0$ (a) and $B = 0.8$ T (b).

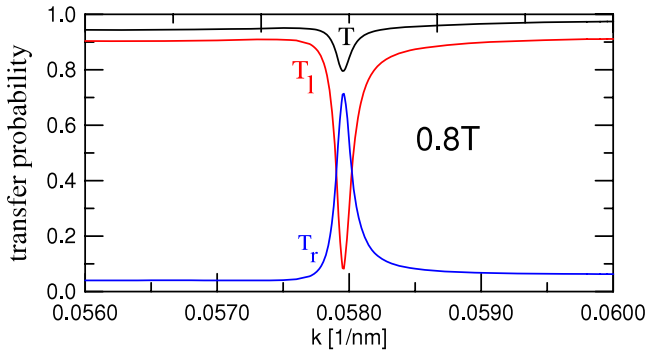

Figure 5. Zoom of a fragment of figure 4(b).

2.6. Transfer probabilities to the left and right output channels

We need to separate the electron transfer probability to the left T_l and right T_r leads of the total transfer probability $T = 1 - R$. For this purpose we calculate the probability currents in the left and right output leads at the top of the computational box. Formula (9) with the boundary condition (8) gives

$$j_l(x) = \frac{\hbar}{m^*}|\Psi(x, y')|^2(\hbar k_l + eBx) \tag{15}$$

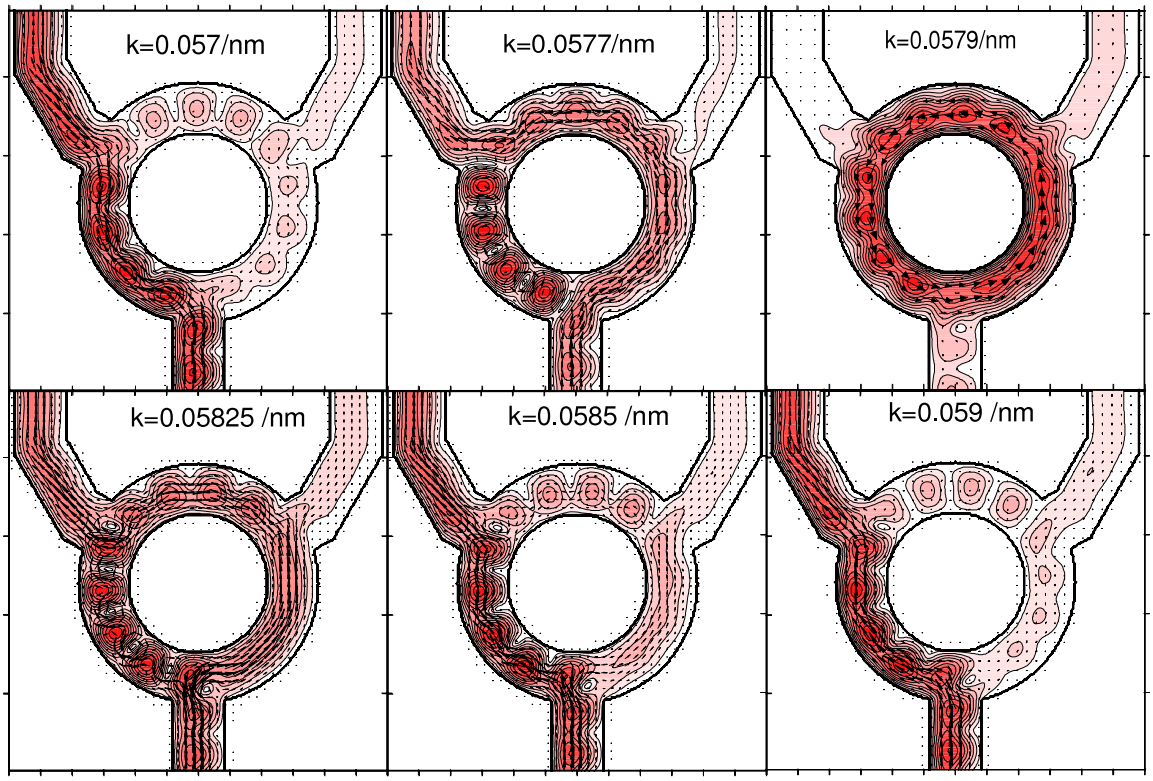

Figure 6. The red contours show the absolute value of the wavefunction (the darker the shade of red, the larger $|\Psi|$) and probability current field (arrows) for $B = 0.8$ T and several values of k indicated at the top of the figure. For the transfer probabilities see figure 5.

for the left lead, and

$$j_r(x) = \frac{\hbar}{m^*}|\Psi(x, y')|^2(\hbar k_r + eBx) \tag{16}$$

for the right one, where y' is the coordinate of the top of the computational box. We integrate the current fluxes on the left and right sides of the box $J_l = \int_{-120\Delta x}^{0} \mathrm{d}x\, j_l(x)$ and $J_r = \int_0^{120\Delta x} \mathrm{d}x\, j_r(x)$. The transfer probability to the left and right channels is then calculated as $T_l = T\frac{J_l}{J_l+J_r}$ and $T_r = T\frac{J_r}{J_l+J_r}$.

2.7. Time-dependent simulations

For the interpretation of the results it is useful to consider also the solution of the time-dependent Schrödinger equation, $i\hbar\partial\Psi/\partial t = H\Psi$. For the initial condition we use a Gaussian wavefunction entirely localized in the input lead

$$\Psi(x, y, t = 0) = \frac{\Delta k^{1/2}}{(2\pi)^{1/4}}\psi_k(x)\mathrm{e}^{-\frac{\Delta k^2}{4}(y-Y)^2+Iqy}, \tag{17}$$

where Y lies far enough below the ring in the incoming lead. Probability density of the initial condition in the wavevector space is

$$|\Psi(k)|^2 = C\exp(-2(k-q)^2/\Delta k^2). \tag{18}$$

The time-dependent calculations are performed using the Crank–Nicolson scheme with a time step of 0.3 fs. We use the finite difference Hamiltonian (3) with the same mesh spacings as in the time-independent calculation, but with radically enlarged computational box. For the time-dependent simulation the computational box that we use covers as much as 12 μm of the input and the output channels. A

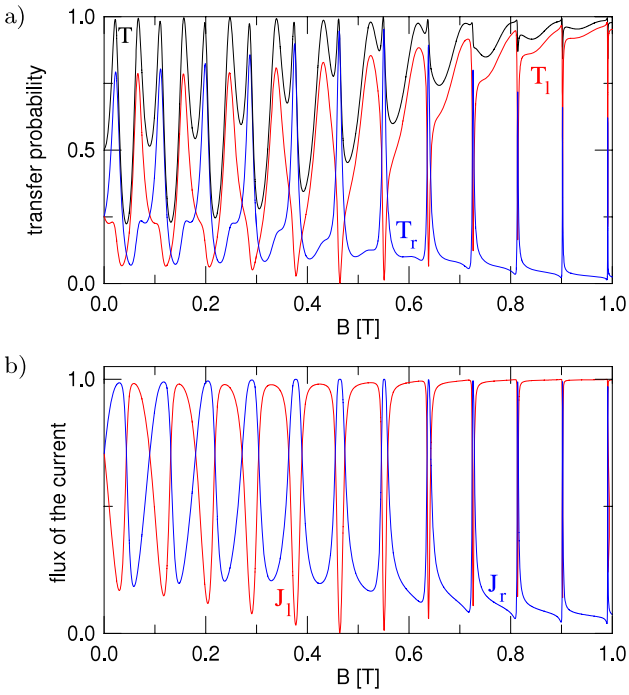

Figure 7. (a) Transfer probabilities to the left T_l and right T_r output channels and their sum T as functions of B for $k = 0.0683$ nm^{-1}. (b) The flux of the current through the left and the right arms of the ring.

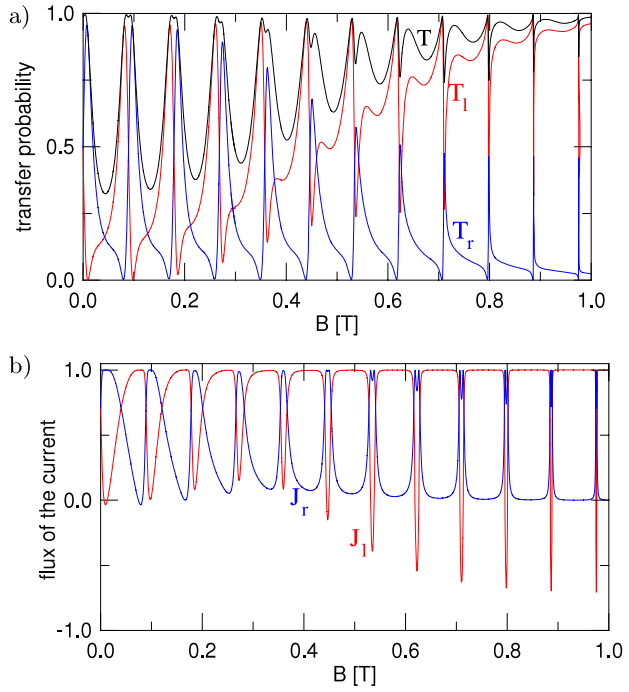

Figure 8. The same as figure 7 but for $k = 0.0667$ nm^{-1}.

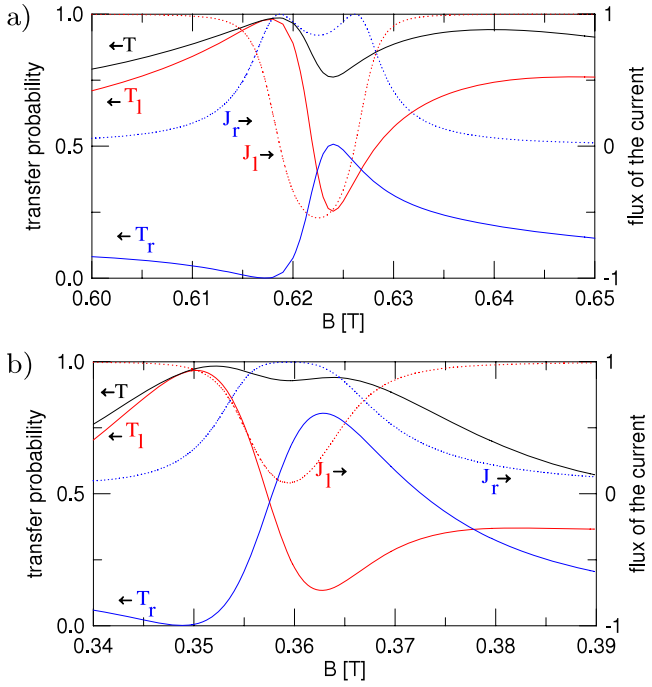

Figure 9. Zoom of two fragments of figure 8 corresponding to T_r maxima. The solid lines show the transfer probabilities (left vertical axis), and the dotted ones the normalized flux of the probability density current through the left and right arms of the ring (right vertical axis).

computational box of this large size was necessary for setting the initial condition for a nearly monoenergetic wavepacket.

2.8. Simulation of the temperature effects for broadening of the transport window

In order to estimate the effects of non-zero temperature for the transport we apply the linear response formula for the conductance [30]

$$G = \frac{2e^2}{h}\bar{T}, \tag{19}$$

with

$$\bar{T} = \int T(E)\left(-\frac{\partial f}{\partial E}\right)\mathrm{d}E, \tag{20}$$

and the Fermi function $f = (\mathrm{e}^{(E-E_\mathrm{F})/k_\mathrm{B}\tau} + 1)^{-1}$, where τ stands here for the temperature. Formula (20) accounts for averaging the transfer probability obtained in the Hamiltonian eigenstates within the transport window that is opened near the Fermi level by thermal excitations. In the integral over the energy the wavevector k corresponding to a given E is found from the eigenequation (6).

3. Results and discussion

3.1. Results for 0 K

Calculated transfer probabilities as functions of the wavevector are presented in figure 4. For $B = 0$ one obtains $T_\mathrm{l}(k) = T_\mathrm{r}(k)$ due to the symmetry of the structure (figure 4(a)). Non-zero magnetic field introduces asymmetry in the transfer probabilities (figure 4(b)). Generally, at $B > 0$ one observes that T_l is enhanced at the expense of T_r, which is consistent with the orientation of the Lorentz force. Nevertheless, for discrete values of k sharp dips of T appear at higher B (figure 4(b)). The dips of T coincide with the minima of T_l and peaks of T_r. A zoom of one of the T dips is shown in figure 5. The amplitude of the wavefunction and probability current distribution for k near the dip are displayed in figure 6. For $k = 0.057$ nm^{-1} the electron is directed to the left arm of the ring and then to the left output channel as previously described by the time-dependent calculations [17–19]. For $k = 0.0577$ nm^{-1} the current forms vortices in the left arm and the actual electron transfer occurs through the right arm of the ring. For $k = 0.0577$ nm^{-1} the current goes through the right arm but the electron transfer to the right lead still has low probability. For $k = 0.0579$ nm^{-1}—at the centre of the T_l dip (T_r peak)—the current forms a giant counterclockwise vortex around the entire ring. A minimum of the wavefunction amplitude is formed at the centre of the entrance to the left output channel—similar to the one observed for $k = 0.0577$ nm^{-1} at the right output channel. For larger k the current starts to flow through the left arm again as guided by the classical magnetic forces.

The magnetic forces influence the distribution of the charge density within the ring. In figure 6 we observe a distinct shift of the wavefunction amplitude with respect to the axes of the channels correlated with the direction of the current and consistent with the orientation of the Lorentz force. For $k = 0.057$ nm^{-1} the wavefunction is distinctly shifted to the left edge of the input and the output channels as well as to the external edge of the left arm of the ring. For $k = 0.0577$ nm^{-1}, when the transfer of the current through the left arm is blocked, the wavefunction maxima

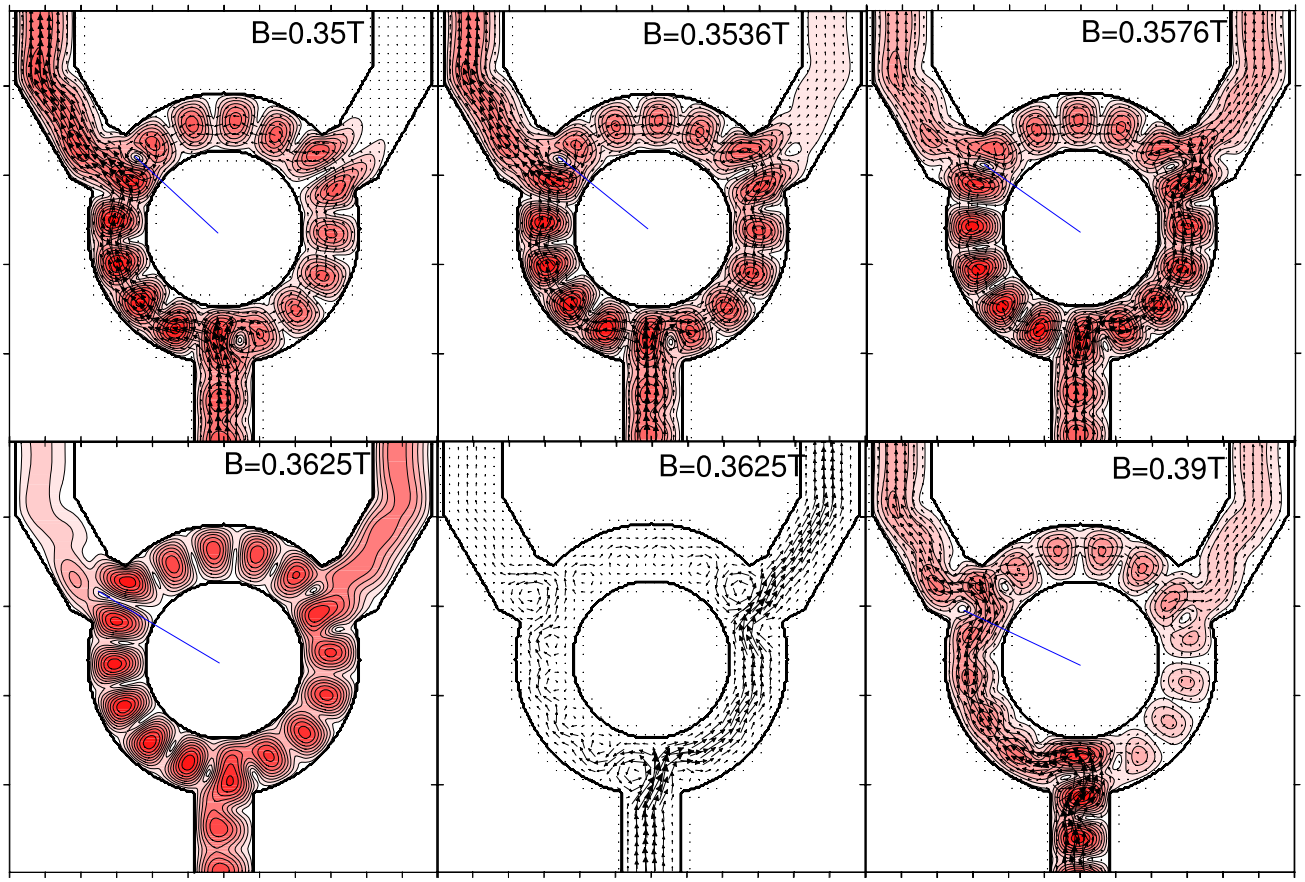

Figure 10. The contour plot shows the absolute value of the wavefunction (the darker the shade of red, the larger $|\Psi|$) and probability current field (arrows) for $k = 0.0667$ nm^{-1} and values of the magnetic field of figure 5(b).

between the input and left output lead are placed symmetrically between the internal and external edges of the ring. For the giant anticlockwise vortex found for $k = 0.0579$ nm^{-1} the wavefunction is pushed to the inner edge of the ring.

In experiments the conductance is usually measured as a function of the magnetic field. Figure 7(a) shows the transfer probabilities as functions of B for $k = 0.0683$ nm^{-1}. At low B the maxima of T correspond to interlaced peaks of T_l and T_r. At higher B the value of T_l increases on average and the peaks of T_r become very narrow. Pronounced dips of T_l are formed at the positions of T_r maxima. The peak/dip structure occurs periodically with the spacings of $\Delta B = 0.09$ T, which corresponds to the flux quantum threading the one-dimensional ring of an effective radius 121 nm that agrees well with the geometry of the model structure (figure 1).

In order to quantify the direction of the current flow within the ring we calculate the flux of the current at the horizontal cross section of the arms of the ring $y = 240$ nm (see figure 1). The fluxes are then normalized to obtain $J_\mathrm{l}^2 + J_\mathrm{r}^2 = 1$. In figure 7(b) we notice that for larger B outside T dips nearly all the current goes through the left arm of the ring.

Figure 8 corresponds to $k = 0.0667$ nm^{-1}, for which a maximum of $T = 2T_\mathrm{l} = 2T_\mathrm{r}$ is found for $B = 0$ (see figure 4(a)). At low B the peaks of T_l and T_r appear very close to one another, forming a wider T maxima. For higher B (i) the maxima of T_r turn into narrow peaks, which coincide with the dips of T_l, and (ii) outside the T dips the current flows up through the left arm of the ring while the current flux through the right arm is close to zero, as discussed above for $k = 0.0683$ nm^{-1}.

Enlarged fragments of figure 8 corresponding to two dips of T_l are shown in figure 9. The amplitude of the wavefunction and the probability density current for the B range of figure 9(b) are illustrated in figure 10. For $B = 0.35$ T the transfer probability to the left lead is maximal, while T_r is minimal. The current goes nearly entirely by the left arm. Note the pronounced elongated minimum of the wavefunction at the exit to the right output channel. This wavefunction would be effectively coupled to the second subband of the right channel, but the latter corresponds to a much higher energy, so the transfer to the right lead is blocked. For $B = 0.3536$ T a leakage of the current to the right lead is observed and J_r becomes equal to J_l. For $B = 0.3576$ T the vortices of the current appear in the left arm. The transfer of the current through the left arm is nearly blocked. Note the position of the sharp minimum of the wavefunction near the left output lead marked by the blue line in figure 10. As B grows from 0.35 T the minimum is shifted to the left and for $B = 0.3625$ T it is found at the centre of the junction of the left output channel to the ring. For this value of the magnetic field T_l becomes minimal. Generally in our simulations a minimum of the wavefunction amplitude at the centre of the junction

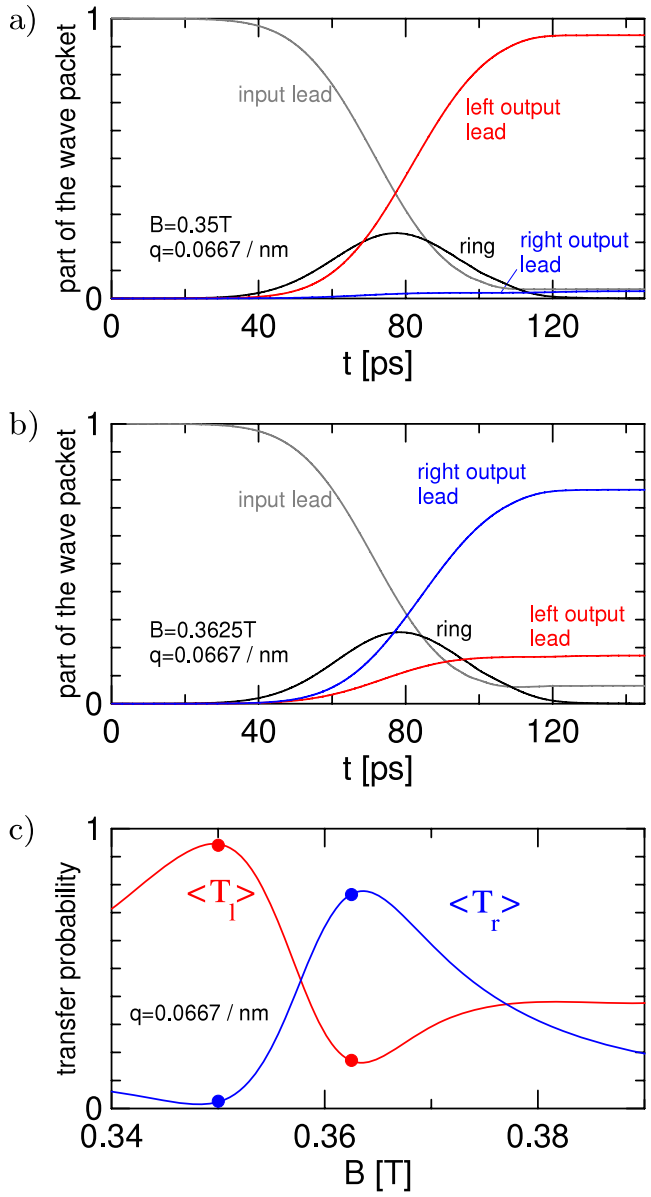

Figure 11. Parts of the wavepacket in the input and the output leads as well as within the ring for $q = 0.0667$ nm^{-1} in the magnetic field of $B = 0.35$ T (a) and 0.3625 T (b). In (c) the lines show the transfer probabilities as functions of the magnetic field obtained by a time-independent calculation in which the transfer probabilities are averaged over the Gaussian distribution corresponding to the wavepacket (equation (21)). The dots show the results of the time-dependent calculation: the parts of the wavepacket that are found in the output leads at the end of simulation for both B considered in (a) and (b).

to the left output lead is found for all minima of T_l which become sharp at higher B. When the electron transfer to the left lead is blocked or hampered, the current goes to the right output channel, leading to appearance of a maximum of T_r. For $B = 0.3625$ T the current forms vortices in the left arm as well as between the output leads, and the main electron transfer goes through the right arm to the right output lead. For $B = 0.39$ T the minimum of the wavefunction is shifted to the lower edge of the left junction and the current transfer through the left arm to the left output channel restarts.

For $J_r > J_l$ the direction of the current circulation is opposite to the one preferred by the Lorentz force. Intervals of B corresponding to this orientation of the current become narrow at higher field (see figures 7(b) and 8(b)). The magnetic field interval for which $T_r > T_l$ also becomes narrower at higher field (see also figure 9).

In order to conclude this section we note that at higher magnetic field the electron transfer goes predominantly through the left arm of the ring to the left output lead, as should be expected due to the orientation of the Lorentz force. For narrow intervals of k or B, wavefunction interference within the ring leads to formation of a wavefunction minimum at the entrance to the left output channel, which blocks the transfer to the left lead. The T_l minima are associated with reversal of the current circulation and appearance of T_r maxima, which turn into sharp peaks at higher B.

3.2. *Wavepacket simulation*

The results presented so far indicate that for some intervals of the magnetic field the current flows in the opposite direction to the one indicated by the Lorentz force. The results of the wavepacket simulation for nearly definite values of the packet wavevector should provide transfer probabilities close to the ones found for the Hamiltonian eigenstates. However, by the Ehrenfest theorem in the wavepacket dynamics the average values of electron momentum and position follow classical laws. Hence, for $B > 0$ a preferential injection of the packet into the left arm of the ring is should be expected for any magnetic field, in contrast to the anomalous current injection that is found for Hamiltonian eigenstates for some values of B. In order to inspect this contradiction more closely we performed wavepacket simulations, in which we assume $\Delta k = 5.5 \times 10^{-4}$ nm (see equation (17)). This wavevector dispersion for the studied structure and $k_F = 0.0667$ nm^{-1} corresponds roughly to the thermal widening of the transport window which occurs at 150 mK. The spatial spread of the initial wavefunction is then as large as 4 μm, and we localize the wavepacket $Y = -8$ μm below the ring in the initial condition (equation (17)).

Figures 11(a) and (b) show the parts of the wavepacket in the leads and within the ring for $B = 0.35$ and 0.3625 T. In figure 11(b) we notice an enhanced packet transfer to the right output lead in consistence with figure 9(b). Figure 12 shows the snapshots of the wavefunction amplitude and the probability current distributions for $B = 0.3625$ T. When the wavepacket enters the ring more of the electron wavefunction goes into the left lead ($t = 43.5$ and 49.3 ps). At $t = 70$ ps an elongated wavefunction minimum is found at the entrance to the left lead. The current flow to the right output lead is visibly enhanced. For $t = 79$ ps the part of the wavepacket inside the ring is maximal and we find that both the wavefunction amplitude and the current distributions are very close to those found in the Hamiltonian eigenstate for $k = 0.0667$ nm (see figure 10 for $B = 0.3525$ T).

Summarizing, in the time-dependent simulations with a nearly monoenergetic wavepacket one first observes an asymmetric injection of the packet to the arms of the ring in accordance with the Lorentz force orientation. Next

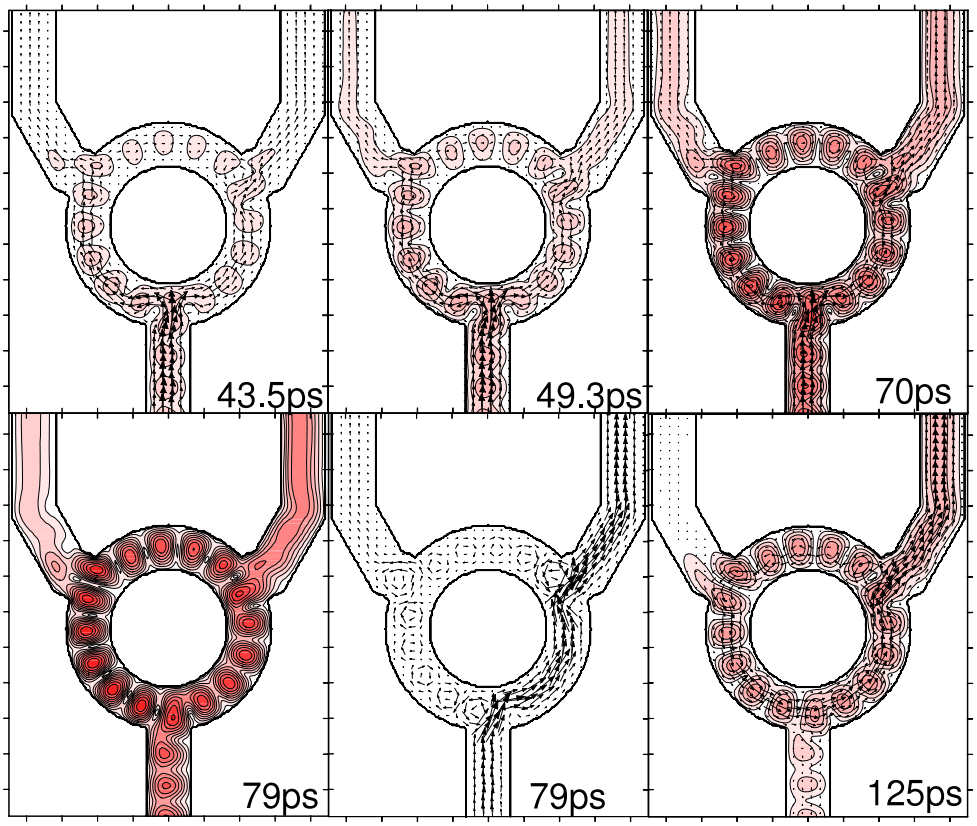

Figure 12. Snapshots of the time-dependent simulation for the average wavevector $q = 0.0667\ \mathrm{nm}^{-1}$ and $\Delta k = 5.5 \times 10^{-4}\ \mathrm{nm}^{-1}$ (see equation (17)) for chosen moments in time. The contour plots show the amplitude of the wavefunction and the arrows—the current distribution. The colour scale for the amplitude is the same for all the plots. The scale for the current vectors is different in each plot.

the interference conditions similar to the ones found in the Hamiltonian eigenstates are formed. For $B = 0.3525$ T the interference blocks the electron transfer to the left lead.

The presented results of the wavepacket simulation were obtained for an extremely low value of Δk. The time-dependent simulations are useful for observation of the enhanced electron transfer to the right lead only for relatively low values of B, before the T_r maxima turn into peaks as sharp as in figure 8(a) for $B = 0.8$ T. The Δk applied here corresponds to roughly one-seventh of the length of horizontal axis of figure 5, which greatly exceeds the width of the T_l dip.

In figure 11(c) we compared the transfer probabilities estimated by the wavepacket simulation with the ones obtained by the time-independent approach after calculating an average over the wavepacket probability density in k space, i.e.

$$\langle T \rangle = C \int \mathrm{d}k\, T(k) \exp(-2(k-q)^2/\Delta k^2). \qquad (21)$$

Figure 11(c) shows that the results of the wavepacket simulations are consistent with the k-vector averaged transfer probability as calculated for Hamiltonian eigenstates.

3.3. Finite temperature effect

At high magnetic field the interference conditions leading to anomalous injection of the current to the right arm of the ring appear for narrow k intervals. The conductance measurements are performed at finite temperatures of the order of 100 mK [20, 31], for which a transport window of a finite width is opened near the Fermi level. In order to study the stability of these anomalous transport conditions at finite temperatures, we performed calculations for averaged transfer probabilities according to equation (20).

For the temperature $\tau = 115$ mK the weight function $-\frac{\partial f}{\partial E}$ calculated for Fermi wavevector[1] $k_\mathrm{F} = 0.0667\ \mathrm{nm}^{-1}$ is nearly a Gaussian function of k centred at k_F with half width $\Delta k = 4.5 \times 10^{-4}\ \mathrm{nm}^{-1}$ for $B = 0$ and $\Delta k = 5.2 \times 10^{-4}\ \mathrm{nm}^{-1}$ for $B = 0.8$ T. In the $B \to \infty$ limit the energy tends to the lowest Landau level for any wavevector, $E(k) \to \hbar\omega_\mathrm{c}/2$, hence the widening of the k window for a given thermal energy $k_b\tau$ at higher B. For $\tau = 350$ mK (700 mK) the corresponding half widths are $\Delta k = 1.4 \times 10^{-3}\ \mathrm{nm}^{-1}$ ($3 \times 10^{-3}\ \mathrm{nm}^{-1}$) and $\Delta k = 1.6 \times 10^{-3}\ \mathrm{nm}^{-1}$ ($3.5 \times 10^{-3}\ \mathrm{nm}^{-1}$), for $B = 0$ and 0.8 T, respectively.

Figure 13 shows the transfer probabilities and normalized current fluxes for Fermi wavevector fixed at $k_\mathrm{F} = 0.0667\ \mathrm{nm}^{-1}$ and three values of the temperature (results for 0 K were given in figure 8). At finite temperature the dips and peaks of the transfer probabilities are transformed into smooth extrema of reduced amplitude, which eventually disappear at high magnetic field. The attenuation of the Aharonov–Bohm oscillations of the transfer probabilities for non-zero

[1] In the present calculation the relation between the wavevectors and energy, k_F and E_F in particular are given by equation (6).

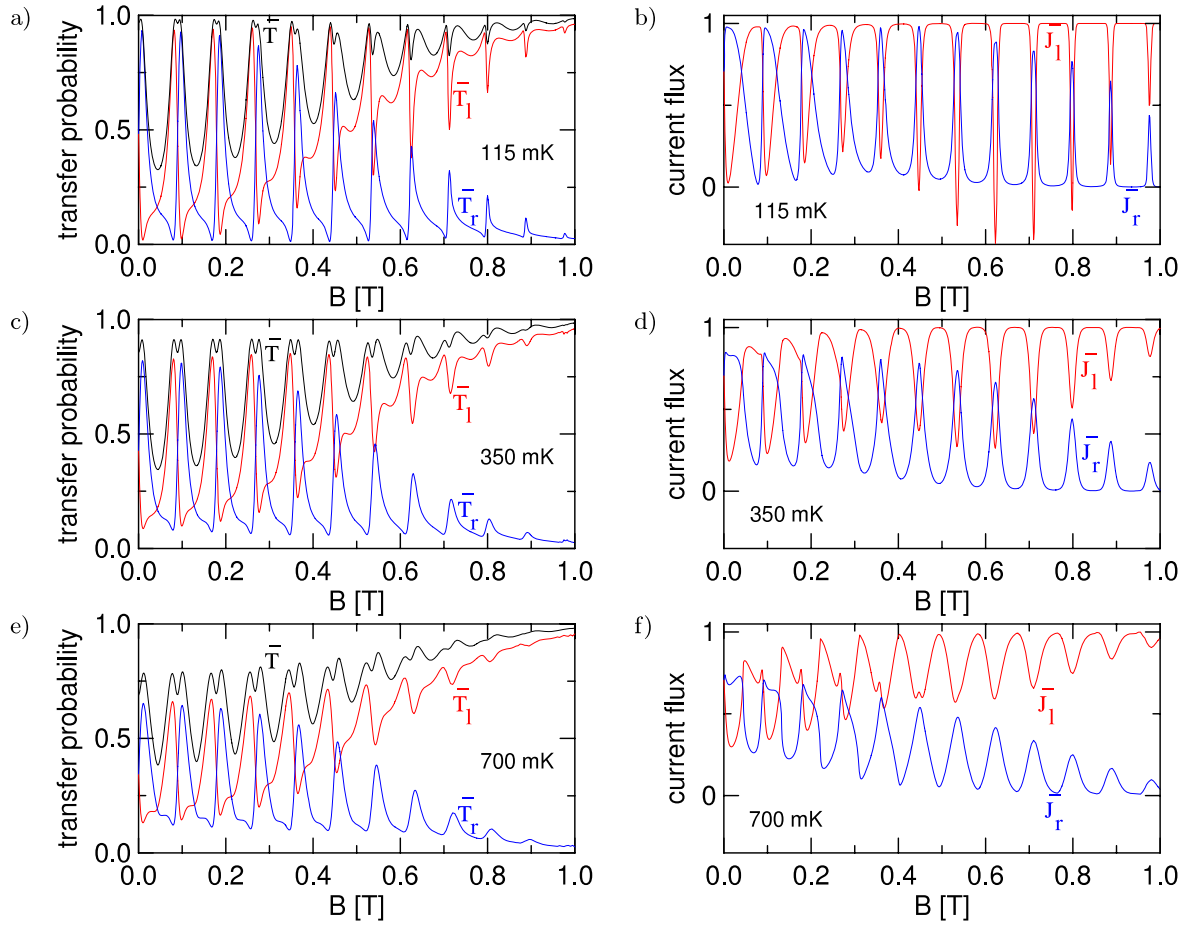

Figure 13. ((a), (c), (e)) Transfer probabilities to the left $\overline{T_l}$ and right output lead $\overline{T_r}$ as well as their sum $\bar{T}$ averaged over the thermally widened transport window for $k_F = 0.0667$ nm^{-1}. ((b), (d), (f)) Normalized current fluxes through the left and right arms of the ring. The results are presented for the temperatures $\tau = 115$ mK ((a), (b)) and 350 mK ((c), (d)) and 700 mK ((e), (f)).

temperatures at higher B is in agreement with the results of previous wavepacket simulations [17–19], in which the averaging of the transfer probabilities with k is embedded in the initial condition. The attenuation was also observed in the experimental data of [20]. Results of figure 13 indicate that the oscillations of the direction of the current circulation around the ring, which determine the orientation of the generated magnetic dipole moment, are more thermally stable than the oscillations of the transfer probabilities, which determine the conductance.

3.4. Ring with a perturbed potential

The experimental results (figure 1 of [20]) indicate a significant anisotropy of the potential landscape within the ring since already at $B = 0$ the conductance of one of the output leads greatly exceeds the other. The appearance of peaks of T_r at high $B > 0$ that we discussed above were associated with specific interference conditions for which the electron wavefunction at the junction to the left output lead possessed a minimum at the axis of the lead (see figure 10 for $B = 0.3625$ T for instance). A question which seems natural is whether such interference conditions are still possible for a quantum ring containing a potential defect.

In order to answer this question we considered a perturbation introduced by Gaussian potential $V_d = W \exp(-[(x - x_c)^2 + (y - y_c)^2]/R_d^2]$, centred at point $x_c = -104.8$ nm $y_c = 179.5$ nm in the left arm just in between the input and left output leads. The size of the defect is assumed to be $R_d = 30$ nm. The results for the transfer probabilities and current fluxes are displayed in figure 14.

For $W = -5$ meV the impurity introduces a potential cavity which mainly shifts the phase of the wavefunction passing through the left arm (figures 14(g) and (h)). We observe no pronounced effect for the qualitative features of the transfer probabilities at high magnetic field as compared to a clean ring $W = 0$ case (cf. figure 8).

A potential barrier that is introduced for $W > 0$ hampers the electron transfer through the left arm. For $W \geqslant 4$ meV the transfer probabilities to the left and right output leads become distinctly different near $B = 0$ (figures 14(c) and (e)), the amplitude of the Aharonov–Bohm oscillation is significantly reduced and the peak/dip structures disappear in the high field limit.

Results of figure 14 for $W = 4$ and 5 meV resemble the measured conductance [20]. Near $B = 0$ the electron transfer goes mainly to the right lead. T_l exceeds T_r only for $B > 0.5$ T. Note that also for $B > 0.5$ T the current

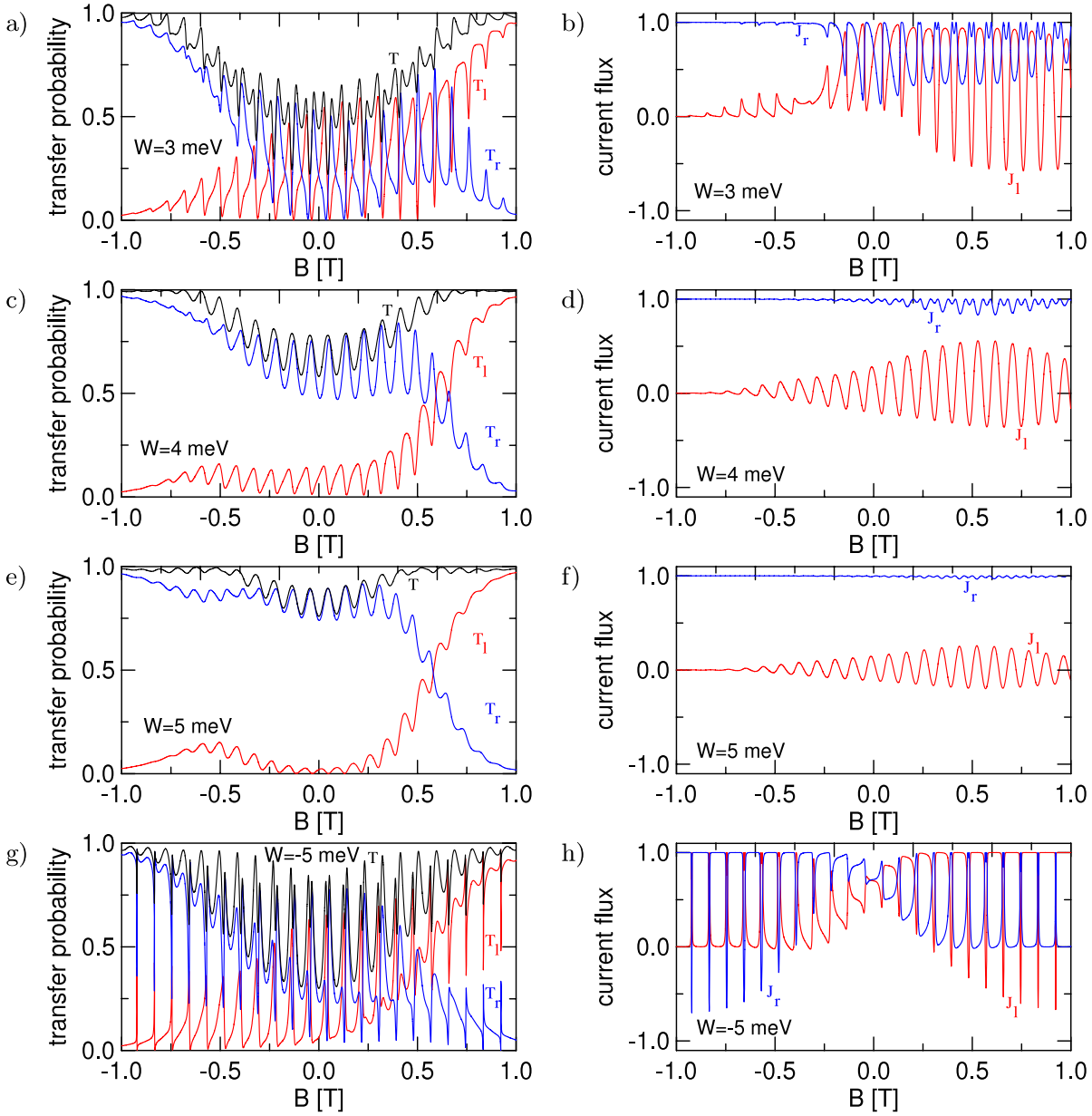

Figure 14. The transfer probabilities and normalized current fluxes for a repulsive potential defect of height 3 meV ((a), (b)), 4 meV ((c), (d)) and 5 meV ((e), (f)). Plots (g), (h) correspond to an attractive defect of depth −5 meV.

flux through the right arm of the ring greatly exceeds the one through the left arm (figures 14(d) and (f)). The dominant electron trajectory for this transport conditions was indicated in [19] using wavepacket simulations.

We conclude that the presence of a repulsive potential defect induces not only the asymmetry of the transfer at $B = 0$ and a weak amplitude of the Aharonov–Bohm oscillation but also the absence of T_r peaks at high B. For a strongly asymmetric potential the peaks of T_r disappear also at zero temperature.

3.5. Ring of an increased channel width

The above results were obtained for the width of the channel within the ring fitted to the width of terminals. For an increased width of the ring channel the electron coming from the lowest subband of the input lead may possess enough energy to occupy locally—i.e. within the ring—the second subband. A local scattering to the second subband may influence the mechanism of the electron transfer through the system. In order to study this point we decreased the inner radius of the ring from 88 to 68 nm (see the inset to figure 15).

The k-resolved transfer probabilities are plotted for $B = 0.8$ T in figure 15. For $k < 0.06$ nm we find similar results to the ones presented above: the transfer goes to the left output lead for nearly each value k. For $k > 0.06$ nm^{-1} the scattering to the second subband of the channel becomes allowed and one observes a non-regular dependence of the transfer probabilities, with T_r exceeding T_l in some intervals. For $k = 0.05$ nm^{-1} (figure 15(b)) the transfer probabilities change with the magnetic field in the same manner as for the ring of smaller width. Very different results are obtained for

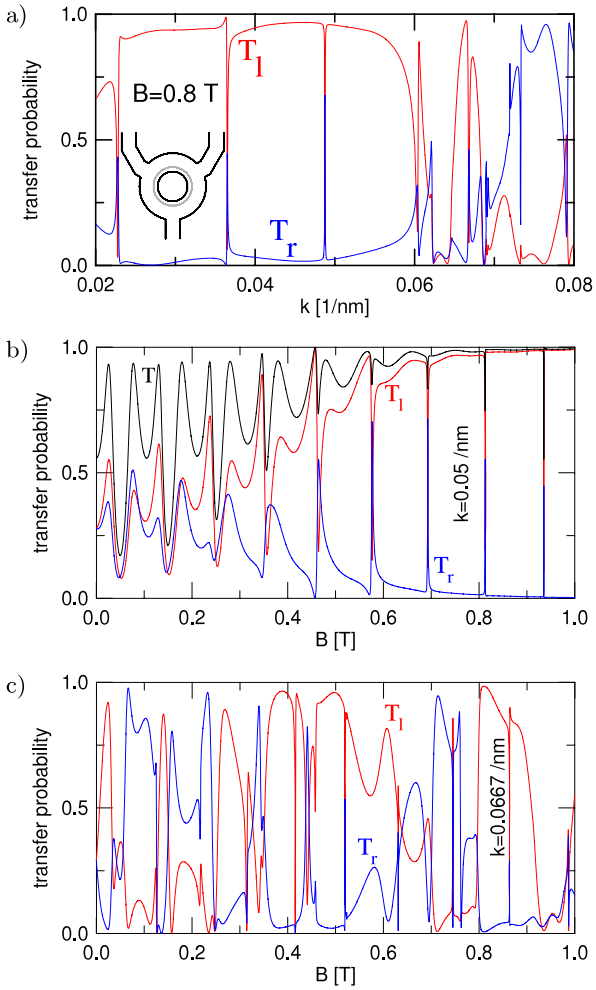

Figure 15. (a) Wavevector resolved transfer probabilities to the left and right output leads for the inner ring radius decreased from 88 nm (grey circle in the inset) to 68 nm (the black circle inside the grey one). Results for the ring channel width equal to the width of the lead channels were presented in figure 4(b). Transfer probabilities as functions of B are plotted for $k = 0.05$ nm^{-1} and 0.0667 nm^{-1} in (b) and (c), respectively.

$k = 0.0667$ nm^{-1} (figure 15(c)). No sign of periodicity can be noticed. The results seem chaotic, with no clear signature of the Lorentz force effect. The results for $k > 0.06$ nm^{-1} resemble the transport through a chaotic cavity (quantum billiard [32]) rather than through a quantum ring.

4. Summary and conclusions

We have discussed the role of magnetic forces in stationary electron flow through a three-terminal quantum ring as obtained for Hamiltonian eigenstates in a single subband transport regime. We have shown that in most cases at high magnetic field the transport seems governed by the magnetic forces: the entire current is injected into the left ($B > 0$) arm of the ring and then ejected to the left output lead, with a transfer probability that tends to 100% at high magnetic fields. Exceptions to this rule are found only for narrow windows of magnetic fields for which interference conditions within the ring lead to formation of wavefunctions which are weakly coupled to the left output channel. This form of interference is associated with anticlockwise circulation of the current within the ring and with an appearance of narrow peaks of transfer probabilities to the right output lead. The anticlockwise circulation is anomalous from the point of view of the direction of classical magnetic forces, since the current is injected into the right and not the left arm of the ring. The sharp peaks of the transfer probability to the right output lead that are found for high B disappear at finite temperatures for which the Aharonov–Bohm oscillations of conductance are eventually attenuated. Oscillations of the current circulation turn out to be more resistant to the thermal widening of the Fermi level than the transfer probabilities. We have demonstrated that the imbalance of the transfer probabilities at $B = 0$ as well as the reduction of the conductance oscillations that are introduced by a scattering centre within the ring are associated with removal of the interference conditions leading to appearance of the peaks of T_r at high magnetic field. We have considered a ring with a width larger than the width of the channels. We demonstrated that, for the wavevectors which allow for appearance of local scattering to an excited subband within the ring channel, the results for conductance become chaotic as a function of B without a clear signature of either the Lorentz force effect or the Aharonov–Bohm oscillations.

Acknowledgments

This work was performed within a research project supported by the Ministry of Science and Higher Education (MNiSW) for 2010–2013. Calculations were performed in ACK–CYFRONET–AGH on the RackServer Zeus.

References

[1] Gefen Y, Imry Y and Azbel M Y 1984 *Phys. Rev. Lett.* **52** 129
Büttiker M, Imry Y and Azbel M Y 1984 *Phys. Rev.* A **30** 1982
Büttiker M, Imry Y, Landauer R and Pinhas S 1985 *Phys. Rev.* B **31** 6207
[2] Webb R A, Washburn S, Umbach C P and Laibowitz R B 1985 *Phys. Rev. Lett.* **54** 2696
[3] Timp G, Chang A M, Cunningham J E, Chang T Y, Mankiewich P, Behringer R and Howard R E 1987 *Phys. Rev. Lett.* **58** 2814
[4] Fuhrer A, Lüscher S, Ihn T, Heinzel T, Ensslin K, Wegscheider W and Bichler M 2001 *Nature* **413** 822
[5] Pedersen S, Hansen A E, Kristensen A, Sorensen C B and Lindelof P E 2000 *Phys. Rev.* B **61** 5457
[6] Keyser U F, Fühner C, Borck S, Haug R J, Bichler M, Abstreiter G and Wegscheider W 2003 *Phys. Rev. Lett.* **90** 196601
[7] van der Wiel W G, Nazarov Yu V, De Franceschi S, Fujisawa T, Elzerman J M, Huizeling E W G M, Tarucha S and Kouwenhoven L P 2003 *Phys. Rev.* B **67** 033307
[8] Mühle A, Wegscheider W and Haug R J 2007 *Appl. Phys. Lett.* **91** 133116
[9] Aharonov Y and Bohm D 1959 *Phys. Rev.* **115** 485
[10] Martins F, Hackens B, Pala M G, Ouisse T, Sellier H, Wallart X, Bollaert S, Cappy A, Chevrier J, Bayot V and Huant S 2007 *Phys. Rev. Lett.* **99** 136807
Pala M G, Baltazar S, Martins F, Hackens B, Sellier H, Ouisse T, Bayot V and Huant S 2009 *Nanotechnology* **20** 264021

[11] Bergsten T, Kobayashi T, Sekine Y and Nitta J 2006 *Phys. Rev. Lett.* **97** 196803
[12] Leturcq R, Schmid L, Ensslin K, Meir Y, Driscoll D C and Gossard A C 2005 *Phys. Rev. Lett.* **95** 126603
[13] Grbić B, Leturcq R, Ihn T, Ensslin K, Reuter D and Wieck A D 2007 *Phys. Rev. Lett.* **99** 176803
[14] Leturcq R, Sánchez D, Götz G, Ihn T, Ensslin K, Driscoll D C and Gossard A C 2006 *Phys. Rev. Lett.* **96** 126801
[15] Gustavsson S, Leturcq R, Studer M, Ihn T, Ensslin K, Driscoll D C and Gossard A C 2008 *Nano Lett.* **8** 2547
[16] Ihn T, Sigirst M, Ensslin K, Wegscheider W and Reinwald M 2007 *New J. Phys.* **9** 111
[17] Szafran B and Peeters F M 2005 *Phys. Rev.* B **72** 165301
Chaves A, Farias G A, Peeters F M and Szafran B 2009 *Phys. Rev.* B **80** 125331
Chwiej T and Kutorasinski K 2010 arXiv:1003.1861
[18] Szafran B and Peeters F M 2005 *Europhys. Lett.* **70** 810
[19] Szafran B and Poniedziałek M 2009 *Phys. Rev.* B **80** 155334
[20] Strambini E, Piazza V, Biasiol G, Sorba L and Beltram F 2009 *Phys. Rev.* B **79** 195443
[21] Földi P, Kálmán O, Benedict M G and Peeters F M 2006 *Phys. Rev.* B **73** 155325
[22] Wu C H and Ramamurthy D 2002 *Phys. Rev.* B **65** 075313
[23] Földi P, Kálmán O, Benedict M G and Peeters F M 2008 *Nano Lett.* **8** 2556
Földi P, Kálmán O and Peeters F M 2009 *Phys. Rev.* B **80** 125324
[24] Pothier H, Lafarge P, Urbina C, Esteve D and Devoret M H 1992 *Europhys. Lett.* **17** 249
[25] Chandrasekhar V, Webb R A, Brady M J, Ketchen M B, Gallagher W J and Kleinsasser A 1991 *Phys. Rev. Lett.* **67** 3578
Mailly D, Chapelier C and Benoit A 1993 *Phys. Rev. Lett.* **70** 2020
[26] Kleemans N A J M, Bominaar-Silkens I M A, Fomin V M, Gladilin V N, Granados D, Taboada A G, Garcia J M, Offermans P, Zeitler U, Christianen P C M, Maan J C, Devreese J T and Koenraad P M 2007 *Phys. Rev. Lett.* **99** 146808
[27] Wilson K 1974 *Phys. Rev.* D **10** 2445
[28] Governale M and Ungarelli C 1998 *Phys. Rev.* B **58** 7816
[29] Büttiker M 1988 *Phys. Rev.* B **38** 9375
[30] Datta S 1995 *Electronic Transport in Mesoscopic Systems* (Cambridge: Cambridge University Press)
[31] Ferrier M, Angers L, Rowe A C H, Guéron S, Bouchiat H, Texier C, Montambaux G and Mailly D 2004 *Phys. Rev. Lett.* **93** 246804
[32] Lüscher S, Heinzel T, Ensslin K, Wegscheider W and Bichler M 2001 *Phys. Rev. Lett.* **86** 2118